Correlation of short-period oscillatory exchange coupling to nanometer-scale lateral interface structure in Fe/Cr/Fe(001)

C. M. Schmidt, D. E. Bürgler,* D. M. Schaller, F. Meisinger, and H.-J. Güntherodt
Institut für Physik, Universität Basel, Klingelbergstrasse 82, CH-4056 Basel, Switzerland
(Received 30 March 1999)

We investigate Fe/Cr/Fe(001) trilayers grown on Ag(001)/Fe/GaAs(001) substrates at different temperatures. By changing the substrate temperature of the bottom Fe film during deposition, but otherwise keeping the preparation parameters constant, we are able to tailor the roughness of the Fe/Cr interfaces. The interfaces are characterized by means of scanning tunneling microscopy (STM). In these differently prepared systems, a clear change of the short-period oscillation amplitude is observed by magneto-optical Kerr effect measurements. A statistical analysis of the STM images allows us to extract the lateral length scale over which the Cr thickness is constant, and it turns out that areas of constant Cr thickness with a diameter larger than 3–4 nm are mandatory for the evolution of short-period oscillations. Two mechanisms are discussed which can explain the observed correlation between structure and magnetism, one linked to the propagation of the coupling through the spacer and the other to the response of the ferromagnetic layers to the transmitted exchange field. [S0163-1829(99)04430-6]

I. INTRODUCTION

Fe/Cr/Fe(001) trilayers and Fe/Cr(001) multilayers were the first systems to exhibit such exciting properties as magnetic interlayer exchange coupling,[1] giant magnetoresistance,[2–4] oscillatory exchange coupling,[4] and short-period oscillatory exchange coupling.[5] Although throughout the last decade Fe/Cr/Fe(001) has served as a model system in the field of thin-film magnetism and by now belongs to the best studied systems both experimentally and theoretically, many questions are still open. In this paper we focus on the short-period oscillatory component of the exchange coupling and in particular on its dependence on the structural properties of the interfaces in symmetric Fe/Cr/Fe(001) trilayers.

It is well known that the structure of the interfaces and thereby the sample preparation procedure has a crucial influence on the coupling behavior. Basically, two experimental approaches have been chosen to tailor Fe/Cr/Fe(001) systems: (i) Fe/Cr(001) bilayers that are grown on Fe(001) whisker surfaces with terraces of a width of approximately 1 μm,[6–8] and (ii) symmetric Fe/Cr/Fe(001) trilayers that are evaporated on other substrate surfaces, in particular, on Ag(001)/Fe/GaAs(001).[9,10] As presented in a previous study,[11] the surfaces of Fe(001) films on Ag(001) are laterally structured on the nanometer scale rather than on the micrometer level. Additionally one has to be careful with respect to chemical cleanness. Similar structural properties have been reported for Fe(001) films grown on other substrates, such as MgO(001).[12]

Common to all approaches and generally accepted is the observation of long-period exchange coupling oscillations of about 10 to 12 monolayers (ML) spacer thickness for growth by sputtering or by molecular-beam epitaxy (MBE) at room temperature, and the appearance of a superimposed short-period oscillatory exchange coupling component of (close to) 2 ML spacer thickness for MBE growth at elevated temperatures on high-quality substrates.

In the whisker system, Pierce *et al.*[6] have demonstrated by means of scanning tunneling microscopy (STM) that Cr grows layer-by-layer at a substrate temperature $T_S = 570$ K. Fe/Cr/Fe(001) systems prepared accordingly exhibit short-period oscillations between ferromagnetic (FM) and antiferromagnetic (AF) coupling, i.e., the alignment of the magnetizations in the two Fe layers changes from parallel to antiparallel and *vice versa*. In the room-temperature case the authors explain and nicely model the vanishing of the short-period oscillations by weighting a short-period oscillation coupling curve with a Gaussian representing the thickness distribution of several exposed layers of the rough room-temperature Cr growth front.

For growth at elevated temperatures on Ag(001)/Fe/GaAs(001) substrates, an exchange coupling contribution favoring a perpendicular arrangement of the magnetizations (90° coupling) is found to dominate. Although several models relate the 90° coupling to thickness fluctuations of the spacer originating from interface roughness,[13–15] little is known about the quality of the Fe/Cr interfaces and the resulting Cr thickness fluctuations.

Therefore, the purpose of the present paper is (i) to present a detailed real-space study of the relevant surfaces occurring during growth of differently prepared Fe/Cr/Fe(001) sandwich structures grown on Ag(001)/Fe/GaAs(001) substrates and (ii) to correlate the specific exchange coupling characteristics to the respective morphological properties.

The paper is organized as follows: in Sec. II information about the instrumentation and experimental procedures is given, and the sample structure is introduced. In Sec. III we present our results concerning the surface morphologies of the bottom Fe(001) layers and the Cr(001) spacer layers together with a comparison of the exchange coupling properties of different samples. In Sec. IV we discuss the results with respect to the correlation of the magnetic and the structural properties.

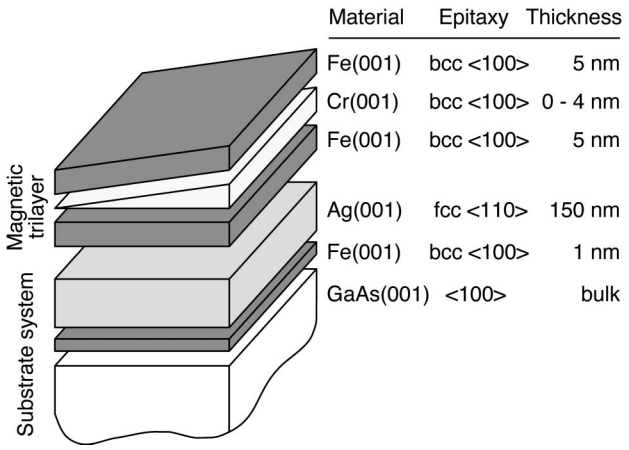

FIG. 1. Layer structure of the Fe/Cr/Fe(001) samples. An Ag(001) buffer layer deposited on Fe-precovered GaAs(001) serves as substrate for the magnetic trilayer. All involved layers are characterized by AES, XPS, LEED, and STM prior to deposition of the subsequent layer. Parallel aligned crystallographic axes in the surface plane defining the epitaxial relationships are given in the table together with the layer thicknesses. The Cr interlayer is wedge-shaped with the slope along a magnetic easy ⟨100⟩ axis of the Fe(001) layers.

II. EXPERIMENTAL

Sample preparation and all measurements, with the exception of Kerr microscopy, are performed in an ultrahigh vacuum (UHV) system with a base pressure of 5×10^{-11} mbar that is equipped with a MBE deposition system, STM, low-energy electron diffraction (LEED), Auger and x-ray photoemission electron spectroscopy (AES, XPS), and a magneto-optical Kerr effect (MOKE) setup which we operate in the usual longitudinal configuration with the external magnetic field applied parallel to a ⟨100⟩ magnetic easy axis of the Fe(001) layers.

Figure 1 depicts a schematic representation of the layer structure of the Fe/Cr/Fe(001) samples, the epitaxial relationships, and the thicknesses of the different films. A 150-nm-thick Ag(001) buffer layer grown on Fe-precovered GaAs(001) wafers at $T_S=380$ K and postannealed at $T_A=570$ K serves as a substrate system for the magnetic trilayers. Recently we have presented a detailed investigation of the morphological properties of the Ag(001) buffer layer:[16,17] STM images reveal terraces with a mean width of approximately 35 nm that are separated by monatomic steps. Most of these steps originate from screw dislocations which are found to be the representative kind of defect in this substrate system. Meanwhile, we have been able to extend the average Ag terrace width by about a factor of 3 by using GaAs(001) wafers which are passivated by an amorphous As cap instead of oxidized GaAs(001) substrates. The As layer is removed *in situ* and a well-defined $c(4\times4)$ reconstruction can be prepared.

The wedge-shaped Cr(001) interlayer with a slope of 0.5 nm/mm and a maximum thickness of 4 nm is grown by linearly moving a shutter in front of the sample during deposition. All STM data of Cr presented in this paper have been recorded at an interlayer thickness $d=2.5$ nm (≈17 ML). The spacer is sandwiched by two 5-nm-thick Fe(001) layers. The whole trilayer is grown at a deposition rate of 0.01 nm/s and the film thickness is controlled by a quartz microbalance. The cleanness of each layer is confirmed by XPS and AES. All morphological, chemical, and magnetic characterizations are performed at room temperature. For the *ex situ* Kerr microscopy analysis the samples are coated with a 5-nm-thick Ag protection layer and with a ZnS layer for the enhancement of the magneto-optical contrast. MOKE measurements in UHV before and after coating with Ag do not show any effect of the cap layer on the width of the plateaus in the hysteresis loops.

TABLE I. Notation and substrate temperature T_S of the Fe/Cr/Fe(001) trilayers. Note that both in the MT_{520} and in the MT_{570} case all Fe/Cr interfaces are formed at 520 K.

Notation	Layer	T_S(K)
RT	Top Fe	300
	Cr	300
	Bottom Fe	300
MT_{520}	Top Fe	520
	Cr	520
	Bottom Fe	100/520
MT_{570}	Top Fe	520
	Cr	520
	Bottom Fe	100/570

In order to be able to study the influence of the Fe/Cr interface morphology on the exchange coupling, we prepare Fe/Cr/Fe(001) sandwich structures by applying three different recipes. They differ from each other by the substrate temperatures during the growth of the Fe and Cr layers. We will use the acronyms RT and MT_T throughout this paper to label the trilayers: RT stands for samples where the whole trilayer is deposited at room temperature. MT_T refers to samples prepared according to a two-stage ''mixed-temperature'' preparation sequence: It involves the evaporation of the first 2 nm of the bottom Fe layer at 100 K and the final 3 nm at $T=570$ K and $T=520$ K, respectively. The Cr interlayer and the top Fe layer are in both cases deposited at 520 K. The notation is summarized in Table I. Because of the low-temperature-growth of the very first atomic layers of both the MT_{520} and the MT_{570} systems, these trilayers are free of Ag substrate atoms.[11] The degree of interdiffusion at the Fe/Cr interfaces found in Refs. 18 and 19 can be expected to be identical for the MT_{520} and the MT_{570} systems since all interfaces are formed at the same temperature (520 K).

III. RESULTS

A. Morphology of bottom Fe(001) layers

A study of the growth of the bottom Fe(001) layer—starting with the RT case, proceeding to elevated temperature growth at $T_S=570$ K, and ending with the optimized two-stage growth procedure MT_{570}—is described in Ref. 11. Here we briefly review RT and MT_{570} Fe films and then extend the study by presenting MT_{520} specimens.

An STM overview image of an RT Fe film is shown in Fig. 2(a). The shape and arrangement of the substrate-

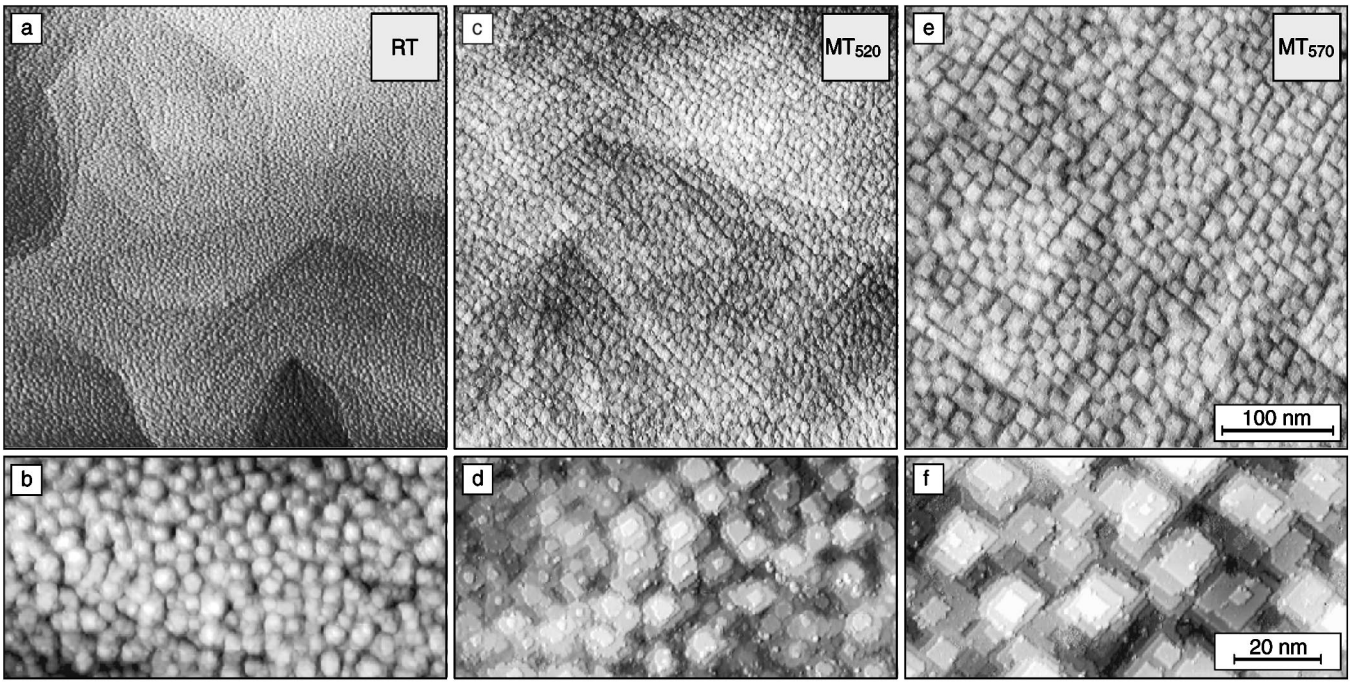

FIG. 2. STM overview images [image size: 400×400 nm^2, (a), (c), (e)] and detail images [image size: 100×50 nm^2, (b), (d), (f)] of 5-nm-thick bottom Fe layers: (a) RT (z range: 4.0 nm), (b) RT (z range: 1.0 nm), (c) MT_{520} (z range: 1.0 nm), (d) MT_{520} (z range: 0.7 nm), (e) MT_{570} (z range: 1.5 nm), (f) MT_{570} (z range: 1.0 nm). The derivative along the fast scan direction has been added to the plane-subtracted raw data for contrast enhancement.

induced steps is very similar to what we observe on the bare Ag(001) surface. However, the terraces between two substrate induced steps are neither structureless nor flat, they are rather covered with hillocks as revealed by the detail image in Fig. 2(b). We statistically quantify the *vertical* roughness of detail images by the rms value $\sigma=\sqrt{\langle z^2\rangle}$ and the *lateral* roughness by calculating the lateral correlation length R. The latter quantity is determined by the position of the first maximum in the pair-correlation function

$$\mathrm{PCF}(r)=\frac{1}{2\pi}\int_0^{2\pi}H(r,\vartheta)d\vartheta, \tag{1}$$

where

$$H(r,\vartheta)=H(\vec{r})=\frac{1}{S}\int_S z(\vec{\rho})z(\vec{\rho}+\vec{r})d^2\rho \tag{2}$$

is the two-dimensional height-height correlation function derived from the surface profiles $z(\vec{r})$ of STM detail images. Thus, R corresponds to the mean separation between typical features, e.g., the hillocks in Fig. 2(b). The integration is performed over the whole image area S. The offset of $z(\vec{r})$ is such that $\langle z\rangle=0$. Therefore, with the normalization chosen in Eqs. (1) and (2) $\mathrm{PCF}(0)=\sigma^2$ holds. In Fig. 3 $\mathrm{PCF}(r)$ calculated from all Fe and Cr STM detail images in Figs. 2 and 4 are displayed. The resulting morphological quantities σ and R are summarized in Table II.

Obviously, Fe grows on Ag(001) at room temperature as a

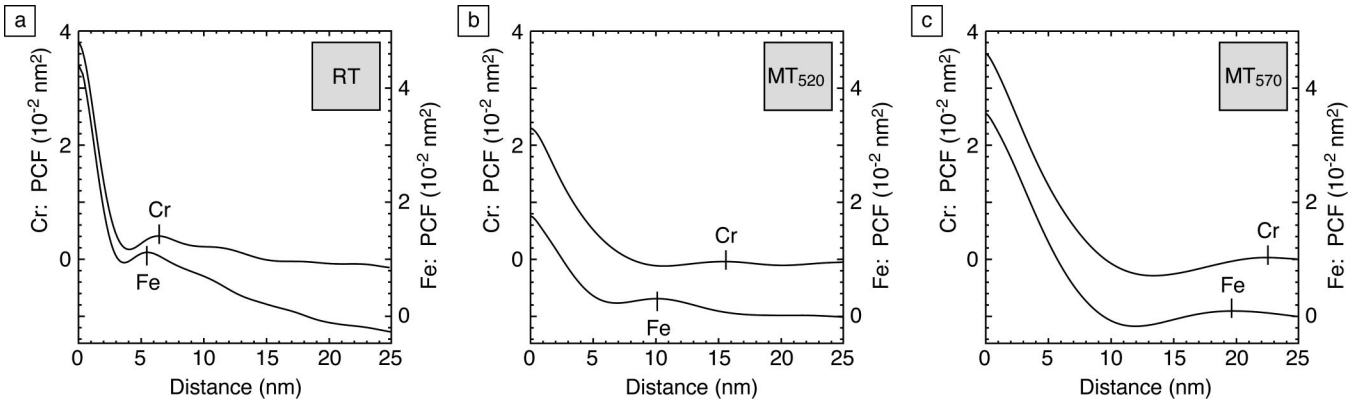

FIG. 3. Pair-correlation functions $\mathrm{PCF}(r)$ calculated from the Fe and Cr detail images of Figs. 2 and 4. For clarity the curves are displayed with an offset: the left-hand (right-hand) vertical axis accounts for Cr (Fe). The position of the labels marks the respective lateral correlation lengths R: (a) RT, (b) MT_{520}, (c) MT_{570}.

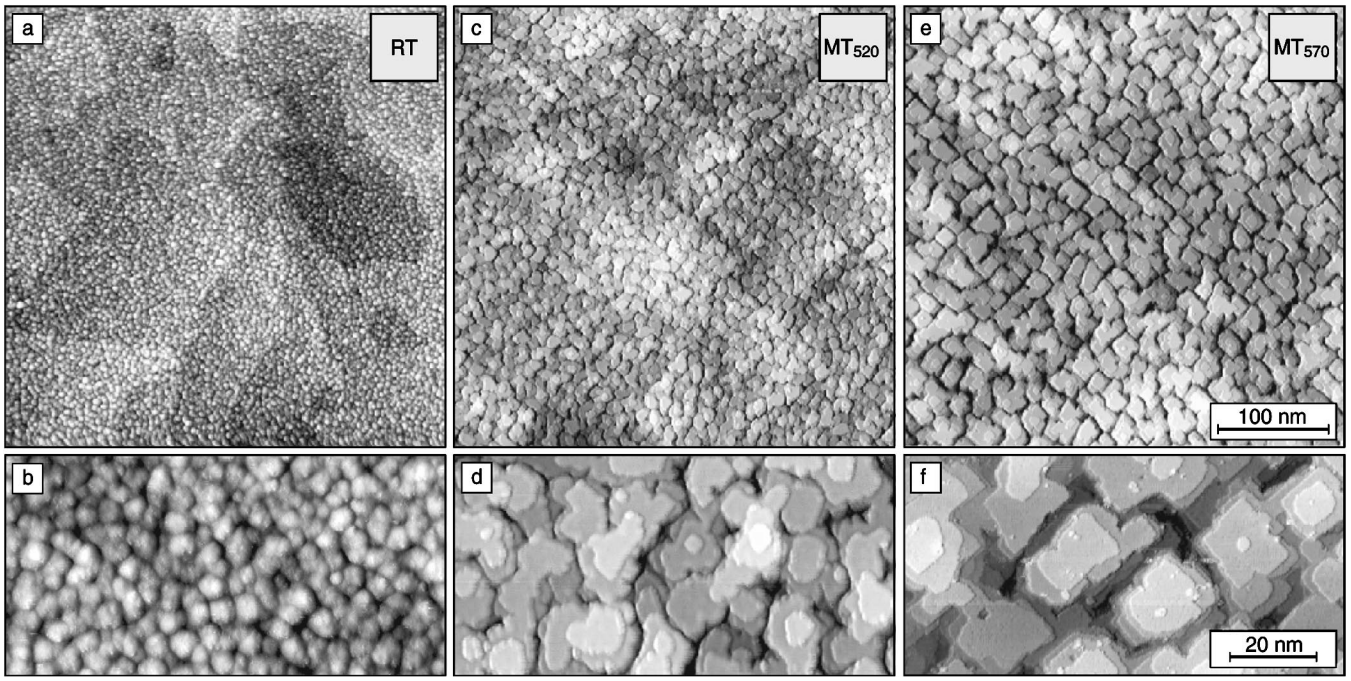

FIG. 4. STM overview images [image size: 400×400 nm^2, (a), (c), (e)] and detail images [image size: 100×50 nm^2, (b), (d), (f)] of the Cr spacer layers recorded at a thickness $d=2.5$ nm: (a) RT (z range: 1.0 nm), (b) RT (z range: 1.0 nm), (c) MT_{520} (z range: 0.7 nm), (d) MT_{520} (z range: 0.7 nm), (e) MT_{570} (z range: 1.5 nm), (f) MT_{570} (z range: 1.5 nm). The derivative along the fast scan direction has been added to the plane-subtracted raw data for contrast enhancement.

continuous film with a rough surface ($R_{Fe}^{RT}=6.1$ nm and $\sigma_{Fe}^{RT}=0.21$ nm). We find that the surface morphology is improved by either growing or postannealing the films at elevated temperatures. However, during deposition at or above room temperature, an atomic exchange process is activated that results in a thin Ag film ''floating'' on top of the growing Fe film (0.2 ML at room temperature and up to 1 ML at elevated temperatures).[11] The exchange is driven by the significantly smaller surface free energy of Ag(001) as compared to Fe(001). Since the mechanism is frozen at 100 K, the MT_{570} growth procedure yields clean and Ag-free surfaces. We argue that the regular morphology with predominantly square-shaped table mountains with single atomic steps running along bcc-Fe(001)⟨100⟩ axes [Figs. 2(e) and 2(f)] represents the intrinsic surface structure of 5-nm-thick Fe films on Ag(001). Driven by the small lattice mismatch between Ag(001) and Fe(001), $m=0.8\%$, it develops even at 570 K, where Fe homoepitaxy proceeds in a near perfect layer-by-layer growth mode.[20] The interface strain can be relieved by the formation of a regular network of ditches with a separation $a_{Fe}/m\approx 38\pm12$ nm, which imposes an upper limit on the lateral correlation length. Note that whereas $R_{Fe}^{MT_{570}}=19.7$ nm has increased by about a factor of 3 compared to the RT case, $\sigma_{Fe}^{MT_{570}}=0.19$ nm has not changed significantly.

TABLE II. Different preparation procedures and the corresponding morphological parameters derived from the STM detail images in Figs. 2 and 4. R measures the lateral correlation length [Eqs. (1) and (2)] and σ is the rms roughness. D denotes the average terrace diameter obtained from Eqs. (8)–(10). σ_Δ calculated according to Eq. (3) stands for the rms fluctuations of the Cr spacer thickness $\Delta(x,y)$. The entries in this table are used in the text with subscripts Fe, Cr, and Δ indicating the bottom Fe layer surface, the Cr spacer layer surface, and the Cr spacer layer thickness, respectively, and superscripts RT, MT_{520}, and MT_{570} referring to the preparation method.

Notation	Layer	R(nm)	σ(nm)	D(nm)	σ_Δ(nm)
RT	Cr	6.8	0.18		0.28
	Bottom Fe	6.1	0.21		
MT_{520}	Cr	15.4	0.16	1.6	0.21
	Bottom Fe	10.1	0.13	1.4	
MT_{570}	Cr	22.4	0.19	1.9	0.27
	Bottom Fe	19.7	0.19	1.7	

Having found an optimized preparation procedure with respect to chemical cleanness and lateral structure size, we now introduce the MT_{520} bottom Fe layer, that additionally offers a possibility to tune the morphological properties without changing the chemical quality. The STM overview image of the MT_{520} bottom Fe layer [Fig. 2(c)] again shows a fairly regular arrangement of table mountains which strongly resembles the surface characteristics of the optimized MT_{570} films. The morphological parameters $R_{Fe}^{MT_{520}}=10.1$ nm and $\sigma_{Fe}^{MT_{520}}=0.13$ nm of the detail image [Fig. 2(d)] are reduced by about one half and one third, respectively, in comparison to their MT_{570} counterparts. The MT_{520} Fe surfaces are also free of Ag.

B. Morphology of Cr(001) interlayers

Qualitatively, the differences of the morphology of the bottom Fe films also show up for the surfaces of the Cr spacer layers, i.e., a rough irregular structure for the RT

preparation [Figs. 4(a) and 4(b)] and a fairly regular arrangement of table mountains for the MT_T preparation methods [Figs. 4(c)–4(f)].

Concerning the RT system, it is impossible from the appearance of the STM images to distinguish between Fe and Cr surfaces: the steps that separate Ag buffer layer terraces are still visible through the Cr/Fe bilayer and cause the large-scale image contrast in Figs. 2(a) and 4(a), whereas locally, the two morphologies are dominated by growth hillocks. $R_{\mathrm{Cr}}^{\mathrm{RT}}$ is slightly larger than $R_{\mathrm{Fe}}^{\mathrm{RT}}$ [Fig. 3 (a)].

Figure 4(e) shows an STM overview image of Cr grown on the MT_{570} Fe surface displayed in Fig. 2(e). The two images strongly resemble each other, and identical rms roughnesses $\sigma_{\mathrm{Fe}}^{\mathrm{MT}_{570}}=\sigma_{\mathrm{Cr}}^{\mathrm{MT}_{570}}=0.19$ nm can be deduced. However, in comparison with the Fe equivalent, the average area covered by a single Cr table mountain appears perceptibly enlarged and the slopes between two table mountains show up steeper [Fig. 4(f)]. The quantitative morphological analysis by means of pair-correlation functions verifies this observation: $R_{\mathrm{Cr}}^{\mathrm{MT}_{570}}=22.4$ nm is significantly larger than the corresponding value of the Fe substrate, $R_{\mathrm{Fe}}^{\mathrm{MT}_{570}}=19.7$ nm [Fig. 3(c)].

The MT_{520} Cr layer [Figs. 4(c) and 4(d)] has smaller and less regular structures than the MT_{570} Cr film [Figs. 4(e) and 4(f)], reflecting the same trend as observed for Fe [Figs. 2(c) and 4(d) in comparison with Figs. 2(e) and 2(f)]. Proceeding in the MT_{520} case from Fe to Cr, both the rms roughness and in particular the lateral correlation length increase considerably from $\sigma_{\mathrm{Fe}}^{\mathrm{MT}_{520}}=0.13$ nm to $\sigma_{\mathrm{Cr}}^{\mathrm{MT}_{520}}=0.16$ nm and from $R_{\mathrm{Fe}}^{\mathrm{MT}_{520}}=10.1$ nm to $R_{\mathrm{Cr}}^{\mathrm{MT}_{520}}=15.4$ nm [Fig. 3 (b)], respectively.

Finally, it is worthwhile noting that the increase of the lateral correlation lengths, i.e., $R_{\mathrm{Cr}}>R_{\mathrm{Fe}}$, both in the RT and in the MT_T systems, has been confirmed by systematic measurements of a large variety of STM images.

C. Exchange coupling of Fe/Cr/Fe(001) trilayers

A magnetization curve in units of the saturation magnetization M_S taken at an interlayer thickness $d=2.5$ nm is shown in the inset of Fig. 5. The shape of the loop is typical for MT_T samples: It reveals the characteristic plateaus at $M/M_S\approx\pm0.5$ resulting from 90° coupling at small external fields.

Corresponding Kerr microscopy images (Fig. 5) confirm the presence of magnetic domains with shapes typical for 90°-coupled Fe/Cr/Fe(001) specimens in the demagnetized state.[21,22] In particular, the majority of domain walls separating areas with different net magnetizations run along the Fe⟨100⟩ directions in contrast to characteristic walls occurring in FM coupled and AF coupled Fe(001) based systems.

Figure 6 shows a three-dimensional (3D) rendering of 200 hysteresis curves taken along the Cr wedge of a MT_{570} sample. The dominance of 90° coupling for Cr thicknesses larger than about 1.2 nm is evidenced by the clearly developed plateaus at $M/M_S\approx\pm0.5$ and the steep drop of the signal between these plateaus. This representation also shows that it is the width of the 90° plateaus that give rise to oscillations as a function of the spacer thickness.

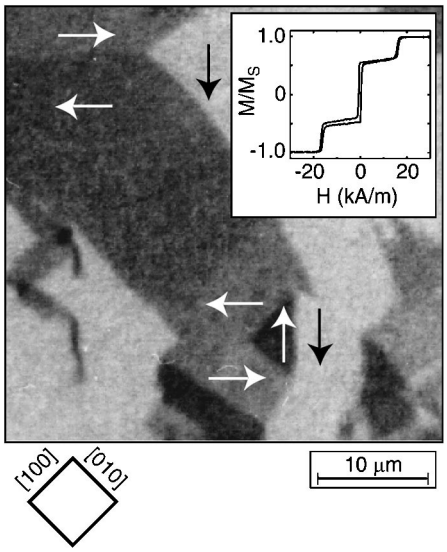

FIG. 5. Kerr microscopy data recorded from the MT_{570} sample in a demagnetized state at $d=2.5$ nm, indicating that the MT_T systems are dominated by 90° coupling (image size: 43×43 μm^2). Arrows refer to the net magnetization resulting from the superposition of the individual magnetizations of the bottom and the top Fe layers (no arrows shown) which are crossed and aligned along ⟨100⟩ magnetic easy axes of the Fe(001) layers. Inset: Corresponding MOKE loop with clearly developed plateaus at $M\approx\pm0.5M_S$ indicating a strong biquadratic coupling contribution.

Given the usual phenomenological energy density *ansatz*[21] with a bilinear coupling term $-J_1(d)\cos(\vartheta)$ parametrizing FM and AF coupling, where ϑ is the angle between the magnetizations of the two Fe layers, and a biquadratic coupling term $-J_2(d)\cos^2(\vartheta)$ favoring the 90° arrangement of the magnetizations, one can estimate the total exchange coupling strength as $J(d)=J_1(d)+J_2(d)=-\mu_0 M_S d_{\mathrm{Fe}} H_S(d)$ by measuring the saturation field $H_S(d)$, defined as half the field interval between the values

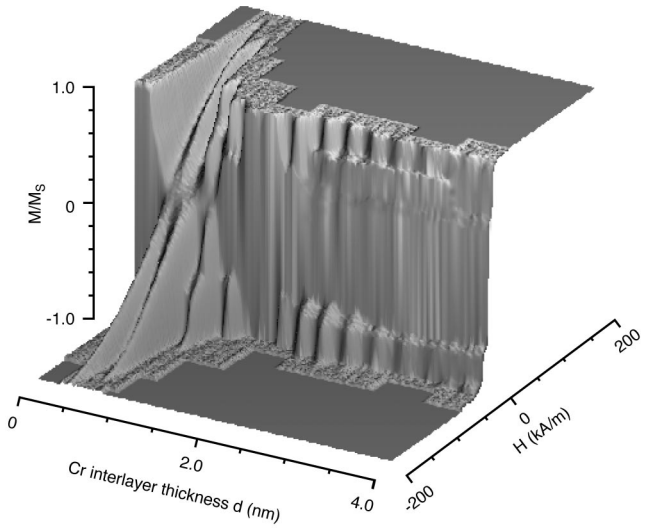

FIG. 6. 3D representation of 200 MOKE hysteresis loops taken at different Cr thicknesses along the Cr wedge of a MT_{570} sample. Each $M(H)$ curve is normalized to its saturation magnetization M_S.

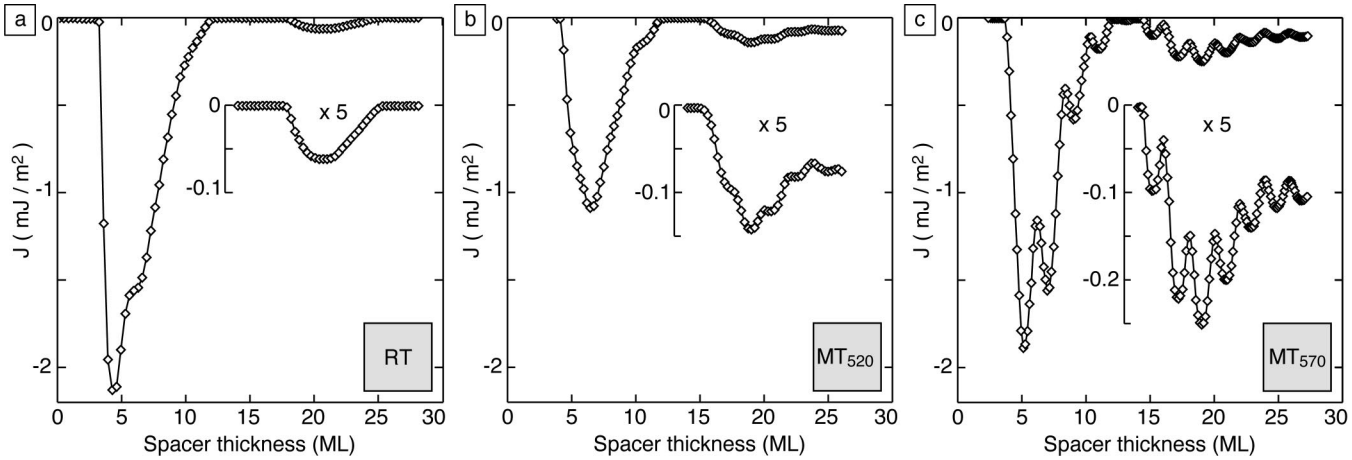

FIG. 7. MOKE coupling curves of Fe/Cr-wedge/Fe(001) trilayers. (a) RT: only long-period oscillatory behavior, (b) MT_{520}: tiny short-period oscillations, (c) MT_{570}: superimposed large-amplitude 2-ML oscillations.

where $M(H)=\pm M_S$. M_S and d_{Fe} denote the bulk saturation magnetization of Fe and the thickness of the Fe layers, respectively. However, this specific contour of hysteresis loops does not allow one to disentangle the bilinear and biquadratic contributions properly. The MOKE exchange coupling curves $J(d)$ taken from the RT [Fig. 7(a)] and the MT_T [Figs. 7(b) and 7(c)] trilayers show a strong dependence on the preparation method. Common to the three systems and in accordance with previous measurements[9] is the strong non-FM background, i.e. $J(d)<0$ for almost all spacer thicknesses. Concerning the MT_{570} system, the appearance of the coupling curve is dominated by the superposition of clear 2-ML oscillations and long-period oscillations of about 12 ML. In the MT_{520} sample only a tiny amplitude $A^{\mathrm{MT}_{520}}$ of the 2-ML oscillatory part remains visible in $J(d)$, whereas in the RT case only the long-period oscillation component survives. From the insets of Figs. 7(b) and 7(c) we determine a ratio of the short-period amplitudes $A^{\mathrm{MT}_{570}}:A^{\mathrm{MT}_{520}}\approx 4:1$ at the Cr thickness of the morphological characterization (i.e., $d=2.5$ nm≈ 17 ML), and $A^{\mathrm{RT}}=0$.

IV. DISCUSSION

A. Spacer thickness fluctuations

The decrease of the lateral correlation length of the bottom Fe layer in the MT_{520} case as compared to the MT_{570} specimen can be explained by the presence of an Ehrlich-Schwoebel barrier:[23,24] Stroscio *et al.*[25] have shown for Fe homoepitaxy on whiskers that a transition from island to near perfect layer-by-layer growth occurs at about 520 K. This transition has been modeled by Amar *et al.*[26] taking into account an Ehrlich-Schwoebel barrier, which causes island growth at room temperature, whereas at elevated temperatures the effect of the barrier becomes less important, enabling layer-by-layer growth. In our case the lattice mismatch between Ag(001) and Fe(001) does not allow pure layer-by-layer growth even at 570 K; rather it limits $R_{\mathrm{Fe}}^{\mathrm{MT}_{570}}$ to an upper, substrate-induced value, whereas smaller structures may develop at 520 K.

From Sec. III it is obvious that the interface structure of the samples has a critical influence on the coupling properties. We emphasize that thickness fluctuations—as is the case for roughness—occur over a certain lateral length scale given by the typical distance between variations in layer thickness. With respect to the 2-ML oscillatory behavior, we are interested in the lateral length scale over which a difference in Cr thickness of *only one monolayer* is to be expected. A determination requires knowledge not only about the morphologies of the two Fe/Cr interfaces, but also about the correlation between them. Because STM is a surface sensitive technique that yields no straight access to buried interfaces, an investigation of the structure of interfaces is generally not trivial. However, as will be shown below, the statistical comparison of STM data taken from the bottom Fe surface and the Cr surface yields a set of real space information from which the Cr thickness fluctuations may be quantified in terms of the rms value and the lateral correlation length.

The quantitative morphological analysis derived on the basis of pair-correlation functions (Table II) shows that for each of the three sample types, R_{Fe} is smaller than and not commensurable to R_{Cr}. As described in Ref. 27 for the RT case, the lateral correlation length in Fe/Cr(001) multilayers increases monotonously with the number of Cr/Fe bilayers at least up to 10 repetitions. Therefore, the roughnesses on both sides of the interlayers cannot be correlated and spacer layer thickness fluctuations of 1 ML are to occur on a lateral length scale smaller than $R_{\mathrm{Fe,Cr}}^{\mathrm{RT}}$. In consistence with this conclusion, Schreyer *et al.*[28,29] arrived from x-ray diffraction measurements performed on a RT $[\mathrm{Cr/Fe(001)}]_5$ sample at a rough estimation of the lateral length scale of constant layer thickness of $\leqslant 1$ nm.

The appearances of the MT_{520} and the MT_{570} Cr morphologies differ from each other, indicating that each type of Cr surface ''memorizes'' its respective lower lying Fe substrate surface. However, the Cr growth front is expected to evolve in a rather complicated fashion: STM measurements by Stroscio *et al.*[30] have proven that a few ML of Cr evaporated at 573 K on flat high-quality Fe whiskers grow perfectly layer-by-layer. An isolated monatomic Fe substrate step edge acts as a sink for the diffusing Cr atoms leading to a denuded region of an irregular contour a few tens of nm wide. The authors speculate that Cr layer-by-layer growth may be inhibited by rough substrates. At the lower substrate temperature of 488 K the Cr growth front reveals several

exposed layers due to the smaller diffusion length. Our nanometer-scale-structured Fe substrate together with the Cr growth temperature of 520 K which is too low to allow true layer-by-layer growth[30] suggests a growth scenario that involves for the initial monolayers a competitive process of (i) partially filling the Fe step edges and (ii) Cr island growth due to the limited diffusion length. For the subsequent atomic Cr layers the latter aspect determines the morphology giving rise to spacer thickness fluctuations. The clearly different lateral correlation lengths, $R_{\mathrm{Fe}}^{\mathrm{MT}_T} < R_{\mathrm{Cr}}^{\mathrm{MT}_T}$ which reflect the incommensurability of the Cr structures with the corresponding Fe structures establish uncorrelated roughness of the two interfaces on the lateral length scale of the table mountains. Note furthermore, that in both cases the top sides of the Cr table mountains do not only cover larger areas but their contours are also smoother as compared to the Fe substrate structures.

Uncorrelated roughness implies that the rms value of the thickness fluctuations of the Cr spacer layer σ_Δ may be calculated from the rms roughnesses of the interfaces by

$$\sigma_\Delta = \sqrt{\sigma_{\mathrm{Fe}}^2 + \sigma_{\mathrm{Cr}}^2}. \tag{3}$$

The results are listed in Table II. $\sigma_\Delta^{\mathrm{RT}} \approx \sigma_\Delta^{\mathrm{MT}_{570}}$, whereas $\sigma_\Delta^{\mathrm{MT}_{520}}$ is found to be somewhat smaller.

From STM measurements of Fe/Cr/Fe(001) whisker systems, Pierce *et al.*[6] extract the rms roughnesses of the Cr spacer layers, which coincide with σ_Δ because for whiskers $\sigma_{\mathrm{Fe}} \approx 0$. In their samples, σ_Δ strongly depends on the growth temperature. The vanishing of the 2-ML oscillations for Cr growth at 320 K is modeled by weighting a coupling curve derived from a 620 K specimen (which is shown to grow layer-by-layer, i.e., with a very small σ_Δ) with a thickness-dependent Gaussian representing the increasing width of the Cr growth front at lower temperatures.

Comparing the RT and the MT_{570} systems, we find almost equal values for $\sigma_\Delta^{\mathrm{RT}}$ and $\sigma_\Delta^{\mathrm{MT}_{570}}$ (Table II). Therefore, a model solely based on the averaging of the coupling strengths by thickness fluctuations as considered in Ref. 6 would lead to the same attenuation of the 2-ML oscillation for both samples, and could not account for our experimental observations. $\sigma_\Delta^{\mathrm{MT}_{520}}$ is even slightly *smaller* than $\sigma_\Delta^{\mathrm{MT}_{570}}$, which should correspond to an *increase* of the amplitude $A^{\mathrm{MT}_{520}}$ of the 2-ML oscillation. However, we observe the opposite: $A^{\mathrm{MT}_{520}}$ is *smaller*.

The clearly different lateral correlation lengths are the obvious distinctions of the three samples, and it seems natural to relate the different coupling curves to this finding, in particular since the R values of all samples reflect the same trend as the amplitudes A of the 2-ML oscillation: $R_{\mathrm{Fe,Cr}}^{\mathrm{RT}} < R_{\mathrm{Fe,Cr}}^{\mathrm{MT}_{520}} < R_{\mathrm{Fe,Cr}}^{\mathrm{MT}_{570}}$ and $A^{\mathrm{RT}} < A^{\mathrm{MT}_{520}} < A^{\mathrm{MT}_{570}}$. However, there is a second difference between the RT and the MT_T preparation procedures: the interfaces are formed at room temperature in the RT case and at 520 K in the MT_T cases. As interface alloying has been observed for Cr growth on Fe(001),[18,19] we cannot exclude chemically different interfaces affecting the coupling behavior. For this reason, we will not go any further into the comparison of RT samples and samples grown at elevated temperatures. From now on we will exclusively focus on the structural and magnetic properties of the MT_T trilayer systems where all interfaces are formed at the same temperature. Note that in the case of interface alloying the STM images of the bottom Fe layer may still be regarded as an approximation of the resulting Fe/Cr interface morphology formed upon progressing in the trilayer fabrication: we assume the chemically diffuse interface to be centered around the STM representation of the topography of the bottom Fe layer. The STM approximation of the upper Fe/Cr interface is supposed to excel that of the lower one, since for this case a chemically sharp interface has been reported.[31]

B. Pillar-and-edge model

We introduce the microscopic interlayer exchange field $H_{\mathrm{ex}}(x,y)$. It is defined as the field experienced by an isolated spin at the lateral position (x,y) in the top Fe layer exclusively due to the presence of the Cr/Fe bilayer underneath. The intrinsic interlayer exchange coupling, i.e., the coupling of an ideal sample with perfect interfaces with a period of two ML, causes a sign change of $H_{\mathrm{ex}}(x,y)$ wherever the spacer thickness varies by an odd number of monolayers. $\mathrm{sgn}[H_{\mathrm{ex}}(x,y)] = +1$ corresponds to FM interaction, and $\mathrm{sgn}[H_{\mathrm{ex}}(x,y)] = -1$ refers to AF coupling. By means of image processing algorithms applied to STM detail images, we aim to extract $\mathrm{sgn}[H_{\mathrm{ex}}(x,y)]$ for the two MT_T systems.

The analysis is illustrated in Fig. 8 for the MT_{570} sample, but it is equally valid for the MT_{520} specimen. For the purpose of noise reduction we start with the discretization of the STM detail images $z_{\mathrm{Fe}}(x,y)$ [Fig. 2(f)] and $z_{\mathrm{Cr}}(x,y)$ [Fig. 4(f)] in units of ML. Figures 8(a) and 8(b) display

$$\mathrm{Int}[z_{\mathrm{Cr}}^{\mathrm{MT}_{570}}(x,y)/l_{\mathrm{Cr}}] + n_{\mathrm{Cr}}, \tag{4}$$

and

$$\mathrm{Int}[z_{\mathrm{Fe}}^{\mathrm{MT}_{570}}(x,y)/l_{\mathrm{Fe}}] + n_{\mathrm{Fe}} \tag{5}$$

respectively, where $\mathrm{Int}(\zeta)$ denotes the integer part of ζ. l_{Fe} and l_{Cr} are the monatomic step heights of Fe(001) and Cr(001), respectively, and the integer constants n_{Fe} and n_{Cr} are chosen to adjust the average layer thicknesses close to the nominal deposition values of 5 nm $\approx$ 35 ML for Fe and $(5 + 2.5)$ nm $\approx (35 + 17)$ ML for Cr, respectively.

Because of the presence of uncorrelated roughness at the two interfaces, a statistical representation of the lateral extent of constant Cr thickness is provided by the subtraction of the lower from the upper interface[32] and leads to the Cr thickness fluctuation image in Fig. 8(c),

$$\Delta(x,y) = \mathrm{Int}[z_{\mathrm{Cr}}(x,y)/l_{\mathrm{Cr}}] - \mathrm{Int}[z_{\mathrm{Fe}}(x,y)/l_{\mathrm{Fe}}] + (n_{\mathrm{Cr}} - n_{\mathrm{Fe}}). \tag{6}$$

Finally, in Fig. 8(d) all areas with spacer thicknesses of an even number of ML are gray-colored, whereas the ones with an odd number of ML are printed in black. Hence, the color code equals a statistical representation of $\mathrm{sgn}[H_{\mathrm{ex}}(x,y)]$ for the MT_{570} sample. Qualitatively, one finds parts in Fig. 8(d) where $\mathrm{sgn}(H_{\mathrm{ex}})$ is a laterally rather rapidly fluctuating function between other parts where $\mathrm{sgn}(H)$ remains constant over larger areas.

Figure 9 presents a cross section of the MT_{570} trilayer derived from line sections taken along the vertically running

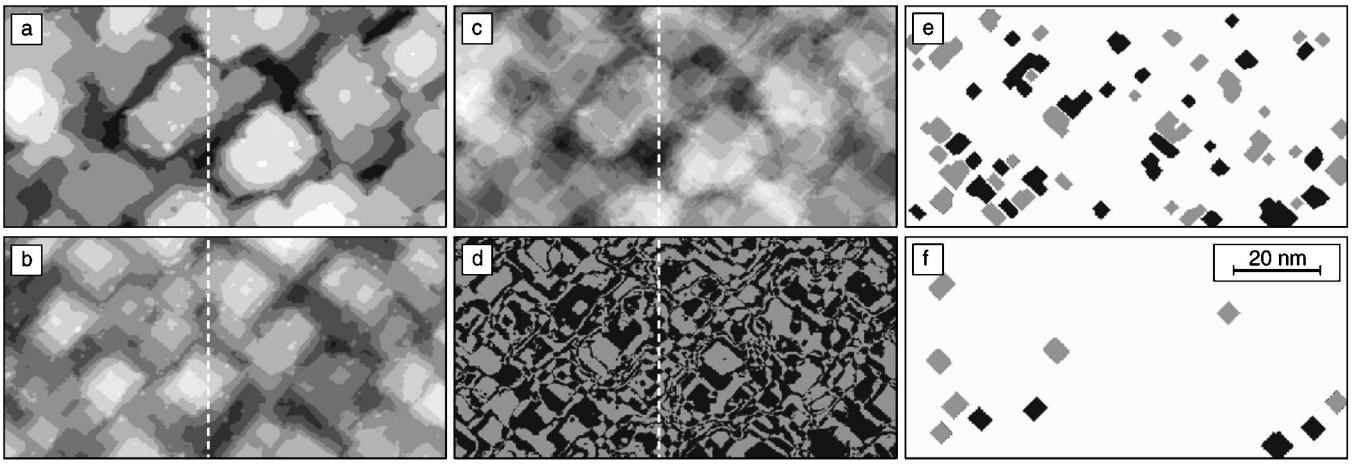

FIG. 8. STM image processing, shown for the MT_{570} system, leading from surface roughnesses to interlayer fluctuations and to pillars with FM- or AF-like character. (a) Discretization image in units of ML of the STM detail image $z_{Cr}^{MT_{570}}(x,y)$ shown in Fig. 4(f) (z range: 8 ML). (b) Same for the detail image $z_{Fe}^{MT_{570}}(x,y)$ of Fig. 2(f) (z range: 6 ML). (c) Statistical representation of the Cr spacer thickness fluctuations $\Delta(x,y)$ calculated by subtracting Fig. 8(b) from Fig. 8(a) (z range: 12 ML). (d) $\mathrm{sgn}[H_{ex}(x,y)]$ derived from Fig. 8(c) indicating spacer thicknesses of even (gray) and odd (black) numbers of ML. (e) Pillars with AF-like character (gray), pillars with FM-like character (black), and the area of the edges (white) for a chosen minimum pillar diameter $\delta = 3.0$ nm. (f) Same for $\delta = 4.0$ nm. Line sections taken along the dashed line (x_0,y) are displayed in Fig. 9.

dashed lines (x_0,y) of Figs. 8(a)–8(d). The two Fe/Cr interfaces (middle two traces) exhibit fluctuations in units of monolayers around their nominal deposition thicknesses. The corresponding curve of Cr spacer thickness fluctuations (bottommost trace) is characterized by sections without any thickness fluctuations [e.g., $\Delta(x_0,y) = 19$ ML for 17 nm $< y < 24$ nm] between sections with frequent fluctuations [e.g., nine steps for 24 nm $< y < 31$ nm]. Since in practice spacer thickness steps higher than one monolayer are negligible, this decomposition matches the sign changes in the microscopic interlayer exchange field (uppermost trace): $H_{ex}(x_0,y)$ is characterized by sections with constant sign [e.g., $\mathrm{sgn}[H_{ex}(x_0,y)] = +1$ for 17 nm $< y < 24$ nm] between sections with frequent sign changes (e.g., nine sign changes for 24 nm $< y < 31$ nm).

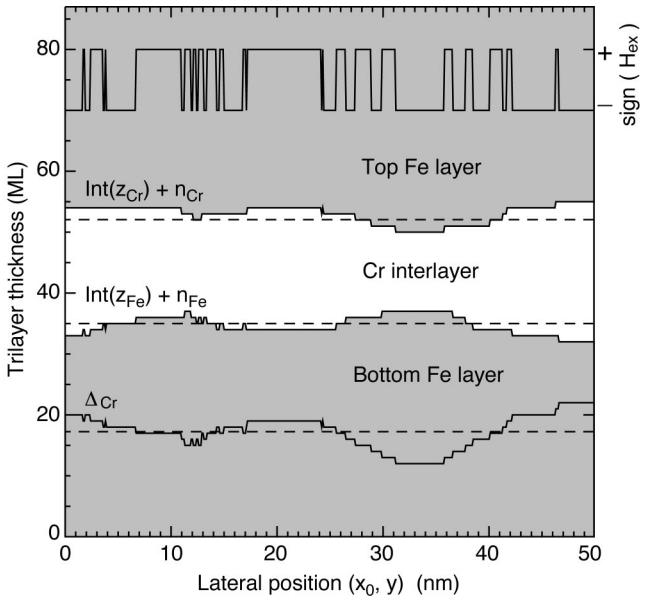

FIG. 9. Cross section of a MT_{570} sample derived from cutting line sections along the dashed lines in Fig. 8 in top-to-bottom direction. The middle two curves represent the fluctuations of the interface morphologies around their nominally deposited thicknesses (dashed lines). The bottommost curve shows their difference, i.e., the fluctuations of the Cr spacer thickness $\Delta(x_0,y)$, whereas the topmost curve, $\mathrm{sgn}[H(x_0,y)]$, is obtained from $\Delta(x_0,y)$ by assuming a sign change at each monostep. The sign convention is in accordance with the measured curve in Fig. 7(c). Note that the vertical length scale is magnified by about a factor of 4 compared to the lateral one.

The schematic picture of a cross section given in Fig. 10 reproduces our STM data for both the MT_{570} and the MT_{520} system in terms of the the lateral decomposition of the Cr spacer layer into parts with no thickness fluctuations which are called *pillars* in the following (hatched areas in Fig. 10) and into other parts with frequent thickness fluctuations, hereafter referred to as *edges*. In order to make this distinction one has to choose a minimum pillar diameter δ. Given

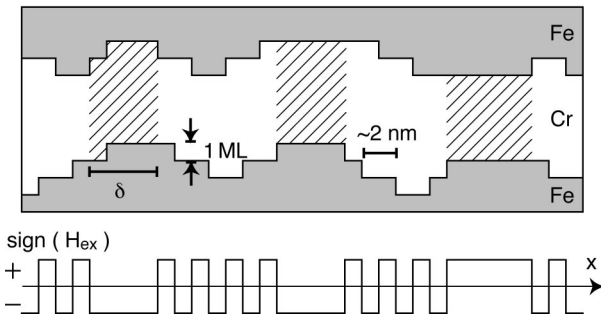

FIG. 10. The pillar-and-edge structure. Schematic cross section of an Fe/Cr/Fe(001) trilayer prepared by the MT_T procedures. In some areas (hatched) with a diameter larger than or equal to δ, the Cr thickness does not fluctuate. Such areas are called *pillars*, whereas the other parts are denoted as *edges*. An AF-like or an FM-like character can be associated with each pillar according to the sign of H_{ex} shown in the lower part of the image.

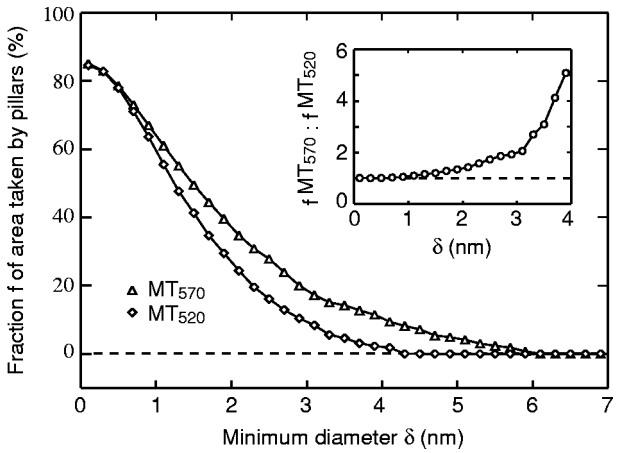

FIG. 11. Fraction f of the spacer area taken by pillars (see text for definition) as a function of δ for the MT_{570} ($f^{MT_{570}}$, $\triangle$) and the MT_{520} ($f^{MT_{520}}$, $\diamond$) sample. Inset: Ratio $f^{MT_{570}}$:$f^{MT_{520}}$ as a function of δ.

an area with constant Cr thickness, only the set union of the compact parts that are large enough to enclose a circle with diameter δ are considered to contribute to the pillar area. All other parts belong to the edges. An AF-like or FM-like character can be attributed to each pillar because in practice the definitions of a pillar by $\Delta(x,y)=\text{const}$ and by $\text{sgn}[H_{ex}(x,y)]=\text{const}$ are equivalent due to a negligible number of biatomic or higher steps.

The character of each pillar changes from FM-like to AF-like and *vice versa* when one ML of Cr is added to the spacer layer, leading to an oscillating behavior as a function of the mean spacer thickness with a period of 2 ML. The amplitude depends on the fraction f of the total area S taken by all pillars. The effect of the pillar height distribution is discussed below. Here it is sufficient to assume that the contributions of all pillars do not completely compensate each other. f is a function of the chosen δ and can directly be determined by image processing algorithms from difference images $\Delta(x,y)$ such as the one displayed in Fig. 8(c) [or equivalently Fig. 8(d)]. The resulting functions $f^{MT_{570}}(\delta)$ and $f^{MT_{520}}(\delta)$ are shown in Fig. 11. They deviate significantly from each other for 1.5 nm$<\delta<$6 nm. The ratio $f^{MT_{570}}$:$f^{MT_{520}}$ (inset of Fig. 11) increases from 2 at $\delta=3$ nm to 5 at $\delta=4$ nm, becomes very large for 4 nm $<\delta<$6 nm because $f^{MT_{520}}\approx 0$, and finally equals 1 for $\delta>6$ nm, where $f^{MT_{570}}\approx 0$, too. If the pillars are to explain the different amplitudes $A^{MT_{570}}$ and $A^{MT_{520}}$ of the 2-ML oscillations in $J(d)$ (Fig. 7), one has to assume a minimum pillar diameter $\delta=\delta_0$ in the range of 3–4 nm. Figures 8(e) and 8(f) show the results of the analysis performed on the MT_{570} specimen for $\delta_0=3.0$ nm and for $\delta_0=4.0$ nm, respectively: with increasing δ_0 a decreasing number of pillars of FM-like character (black) or AF-like character (gray) are surrounded by the growing area contributing to the edges (white).

In agreement with our value of δ_0, x-ray diffraction experiments by Schreyer *et al.*[28,29] revealed a rough order-of-magnitude estimation of the lateral length of constant interlayer thickness of $\leqslant 10$ nm for a $[Cr/Fe]_9$ sample grown at 523 K.

What is the physical meaning of δ_0? Periodic fluctuations

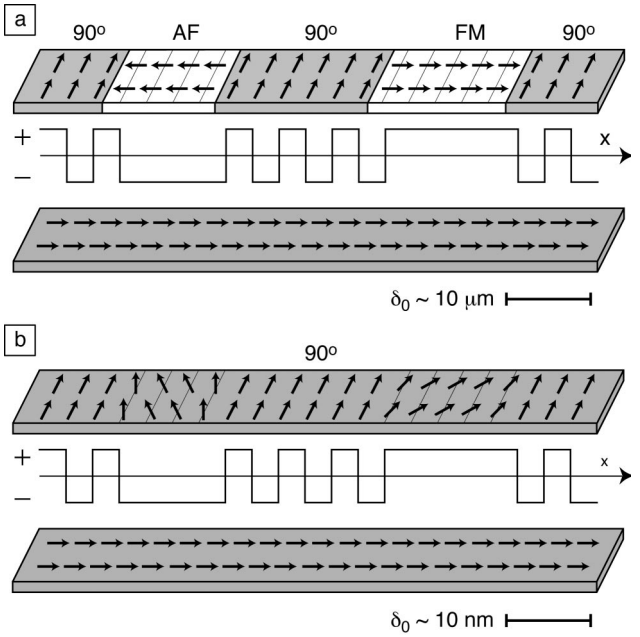

FIG. 12. Schematic response of the top Fe layer to the H_{ex} profile shown between the Fe layers under the assumption of a homogeneously magnetized bottom Fe layer. (a) For δ_0 of the order of micrometers, FM and AF domains develop at the positions of pillars, and 90° domains in between. (b) For δ_0 of the order of nanometers, the spin orientation of the top Fe layer is locally perturbed, resulting in positive or negative angular deviations from the overall 90° coupling. All magnetizations are in-plane.

of $\text{sgn}[H_{ex}(x,y)]$ on a nanometer length scale have been shown by Slonczewski[13] to induce an effective 90° coupling due to the averaging effect of the *intralayer* direct exchange interaction in each of the two Fe layers. Let us first assume that δ_0 is large, e.g., of the order of micrometers. In that case each pillar would give rise to an AF or FM domain in a sea of 90° coupling. This situation is sketched in Fig. 12(a). Note the micrometer length scale. The arrows indicate the direction of the domain magnetization.

As we reduce δ_0, the domains cannot become smaller than the width of the domain walls in the system. For our sample geometry superimposed Néel walls[33] are preferred to uncoupled Néel walls, because the two magnetic layers can efficiently compensate their stray fields in the superimposed configuration. The width $d_{Néel}$ of superimposed walls in FM exchange coupled trilayers has been calculated[34,35] as a function of the intrinsic coupling strength. For Fe/Cr/Fe(001) and the spacer thickness of interest (2.5 nm), $d_{Néel}$ is of the order of 150 nm. $d_{Néel}$ is even larger in the case of AF coupling because the core of the domain wall with antiparallel alignment of the film magnetizations is then stabilized by the interlayer exchange coupling term.

Obviously, the value of δ_0 found in our experiments is at least one order of magnitude smaller than $d_{Néel}$, and we can no longer talk about domains. Instead, we have to consider noncollinear spin configurations in each of the two Fe layers with angular deviations from the perfectly 90°-coupled situation. They are the answer of the system to all competing interactions: intralayer direct exchange, $H_{ex}(x,y)$ due to interlayer exchange coupling, anisotropies, and demagnetiza-

tion. Figure 12(b) sketches this situation. Note the nanometer length scale. The arrows now represent the slowly varying direction of individual spins.

The model sketched in Fig. 12 is confirmed by calculations by Ribas and Dieny:[36] They study numerically 90°-coupling in Fe/Cr/Fe trilayers on samples characterized by different terrace widths D. The important parameter which determines the behavior or the magnetization direction on terraces separated by monatomic steps turns out to be the ratio between the size of the terraces D and l_{wall}, that characterizes the width of the area in which the magnetization is perturbed by the change of sign of the coupling at the border between two semi-infinite terraces. Dependent on the size of the terraces, these authors find either complete FM and AF alignment of the magnetizations on terraces separated by monatomic steps ($D/l_{\mathrm{wall}} \gg 1$) or only small oscillatory deviations of the magnetization direction from an average relative orientation of 90° ($D/l_{\mathrm{wall}} \ll 1$). The amplitude of the deviations decreases with decreasing terrace width. Neglecting anisotropies, the characteristic width of the wall is given by $l_{\mathrm{wall}} = \frac{1}{2}\pi\sqrt{A_{\mathrm{ex}} d_{\mathrm{Fe}}/J_{\mathrm{Cr}}}$, where A_{ex} denotes the exchange stiffness of Fe, d_{Fe} is the thickness of the Fe films, and J_{Cr} is the interlayer exchange coupling at a certain Cr thickness. From Figs. 7(b) and 7(c) we estimate $J_{\mathrm{Cr}} = 0.15$ mJ/m^2 at the spacer thickness of interest (2.5 nm) and obtain $l_{\mathrm{wall}} \approx 38$ nm. Obviously, our samples must be described in a picture with the local spin orientation slightly deviating from the exact 90° alignment as sketched in Fig. 12(b).

The total effect of all pillars within a certain area (e.g., within the laser spot in MOKE experiments), finally, is the sum over all their coupling contributions. The contribution of each pillar is proportional to its height to the power $-\alpha$, where α is the decay exponent of the intrinsic bilinear exchange coupling. This sum is nonzero, except for special and improbable pillar height distributions. Our reasoning assumes that for the spacer thicknesses of interest (15–20 ML) the height distribution function does not change significantly upon adding one ML of Cr, except that the mean pillar height increases by one ML.

In a macroscopic experiment such as MOKE the noncollinear configuration shown in Fig. 12(b) is expected to yield an effective 90° coupling in agreement with our MOKE hysteresis loops and the Kerr microscopy data (Fig. 5). The overall effect of the pillars is a modulation of the biquadratic effective coupling strength as a function of the spacer thickness with a period of 2 ML, which shows up as oscillations in Figs. 7(b) and 7(c).

C. Loss of translational invariance

So far, we have made no specific assumptions about the intrinsic spin structure of the Cr interlayer. Now, we explicitly suppose the presence of paramagnetic Cr. With regard to the ongoing research about the actual intrinsic spin structure of Cr(001) sandwiched by Fe(001) layers, the picture of paramagnetic Cr and pure Ruderman-Kittel-Kasuya-Yosida (RKKY) interaction may prove to be oversimplified, and more quantitative analysis will be needed to adapt the qualitative picture presented below to the true internal Cr spin structure (see, e.g., Ref. 37).

Throughout Sec. IV B we have assumed that $H_{\mathrm{ex}}(x,y)$ is local in the sense that it depends only on the spacer thickness at the position (x,y). In the framework of RKKY interaction Bruno and Chappert[38] have shown that the loss of translational invariance for distances larger than D leads to a finite in-plane coherence length of the electrons of the order of D. If the electrons mediating the coupling have a Fermi velocity component parallel to the interface, the coherence length perpendicular to the interfaces d_{max} is also limited

$$d_{\mathrm{max}} \approx \frac{D}{\tan\gamma}, \tag{7}$$

where γ is the angle between the Fermi velocity and the interface normal. The exchange field is suppressed by destructive interference for spacer thicknesses $d > d_{\mathrm{max}}$. As mentioned by these authors, interface roughness breaks the translational invariance. The in-plane coherence length D can roughly be described by the average diameter of the flat portions of the interfaces.[38] In order to obtain D, we again consider the function $f(\delta)$, which we now determine separately for the Fe and Cr surfaces $z_{\mathrm{Fe}}(x,y)$ and $z_{\mathrm{Cr}}(x,y)$ of the MT$_T$ systems. $f(\delta)$ can formally be written as

$$f(\delta) = \frac{1}{S}\int_{\delta}^{\infty} N(x)\,\pi\left(\frac{x}{2}\right)^2 dx. \tag{8}$$

$N(x)$ is the number of flat portions with diameter x within an image with area S and can be derived from Eq. (8) as

$$N(x) = -\frac{4S}{\pi}\frac{df}{dx}x^{-2}. \tag{9}$$

The average terrace area is

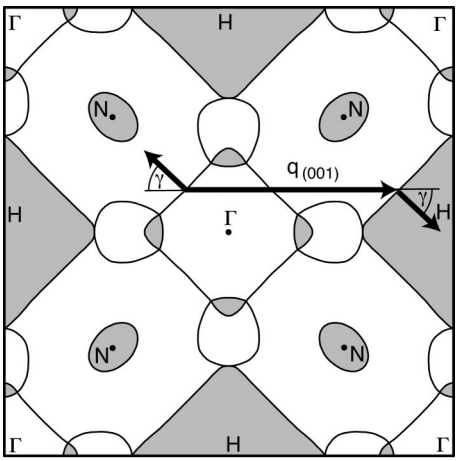

FIG. 13. Fermi surface cross section of paramagnetic Cr in the (001) plane after Ref. 39. The horizontal arrow represents the nesting vector $q_{(001)}$ that gives rise to the 2-ML period of the interlayer coupling. The short arrows indicate the directions of the Fermi velocities of the states connected by $q_{(001)}$. γ is the angle between the interface normal and the Fermi velocities.

$$\pi\left(\frac{D}{2}\right)^2=\frac{\int_{\epsilon}^{\infty}N(x)\,\pi\left(\frac{x}{2}\right)^2dx}{\int_{\epsilon}^{\infty}N(x)dx}=\frac{Sf(\epsilon)}{\int_{\epsilon}^{\infty}N(x)dx}. \qquad (10)$$

The lower integration boundary ϵ is set to 0.5 nm in order to exclude terraces with diameters smaller than two nearest-neighbor separations. The values of D for all four surfaces are listed in Table II. The average diameters of the two interfaces of the MT_{570} and MT_{520} samples are $D^{MT_{570}}=(D_{Fe}^{MT_{570}}+D_{Cr}^{MT_{570}})/2=1.8$ nm and $D^{MT_{520}}=(D_{Fe}^{MT_{520}}+D_{Cr}^{MT_{520}})/2=1.5$ nm, respectively.

Figure 13 shows a Fermi surface (001) cross section of paramagnetic Cr. The 2-ML period of the intrinsic exchange coupling across Cr(001) spacer layers is associated with a nesting vector $|q_{(001)}|=0.95\Gamma H$ that connects the electron and hole pockets of the Cr Fermi surface around the points Γ and H of the bcc Brillouin zone.[40] The Fermi velocities of the states on the edges of the pockets connected by $q_{(001)}$ have an orientation with $\gamma\approx 45°$, giving rise to a coherence length $d_{max}\approx D$. Therefore, the contribution of these states to H_{ex} decays for d larger than D. Hence, this scenario also provides a mechanism to explain the dependence of the amplitude of the short-period oscillation on subtle morphological changes on the nanometer scale.

For our samples $D^{MT_{520}}<D^{MT_{570}}<d=2.5$ nm, and we expect a stronger attenuation of the 2-ML oscillation at $d=2.5$ nm for the MT_{520} preparation compared to the MT_{570} case.

V. SUMMARY

Our experimental data shows a clear dependence of the interlayer exchange coupling on the interface morphologies: short-period oscillations turn up if the Cr spacer contains compact regions of constant thickness (pillars) with diameters larger than $\delta_0=3-4$ nm, and their amplitude increases with increasing lateral extent of these pillars. This observation has been related to two mechanisms which are sensitive to the interface morphology on the nanometer scale: (i) the response of the spin configuration in the magnetic films to the exchange field, and (ii) destructive interference of the electrons mediating the short-period coupling due to the broken translational invariance at the Fe/Cr interfaces. The two mechanisms are expected to occur simultaneously. The first describes the *response of the magnetic layers* to $H_{ex}(x,y)$ in competition with other magnetic interactions, in particular intralayer exchange, whereas the second deals with the *propagation* of $H_{ex}(x,y)$ in the spacer layer.

ACKNOWLEDGMENTS

We thank J. McCord for the Kerr microscopy data and B. O. Fimland for providing us with As-capped GaAs(001) wafers. Financial support from the Swiss National Science Foundation and the Swiss *Kommission für Technologietransfer und Innovation* is gratefully acknowledged.

*Author to whom correspondence should be addressed. Present address: Institut für Festkörperforschung, Forschungszentrum Jülich GmbH, Germany. Electronic address: D.Buergler@fz-juelich.de

[1] P. Grünberg, R. Schreiber, Y. Pang, M.B. Brodsky, and H. Sowers, Phys. Rev. Lett. **57**, 2442 (1986).
[2] M.N. Baibich, J.M. Broto, A. Fert, F. Nguyen Van Dau, F. Petroff, P. Etienne, G. Creuzet, A. Friederich, and J. Chazelas, Phys. Rev. Lett. **61**, 2472 (1988).
[3] G. Binasch, P. Grünberg, F. Saurenbach, and W. Zinn, Phys. Rev. B **39**, 4828 (1989).
[4] S.S.P. Parkin, N. More, and K.P. Roche, Phys. Rev. Lett. **64**, 2304 (1990).
[5] J. Unguris, R.J. Celotta, and D.T. Pierce, Phys. Rev. Lett. **67**, 140 (1991).
[6] D.T. Pierce, J.A. Stroscio, J. Unguris, and R.J. Celotta, Phys. Rev. B **49**, 14 564 (1994).
[7] B. Heinrich and J.F. Cochran, Adv. Phys. **42**, 523 (1993).
[8] B. Heinrich, J.F. Cochran, T. Monchesky, and K. Myrtle, J. Appl. Phys. **81**, 4350 (1997).
[9] J.A. Wolf, Q. Leng, R. Schreiber, P.A. Grünberg, and W. Zinn, J. Magn. Magn. Mater. **121**, 253 (1993).
[10] R.J. Hicken, C. Daboo, M. Gester, A.J.R. Ives, S.J. Gray, and J.A.C. Bland, J. Appl. Phys. **78**, 6670 (1995).
[11] D.E. Bürgler, C.M. Schmidt, D.M. Schaller, F. Meisinger, R. Hofer, and H.-J. Güntherodt, Phys. Rev. B **56**, 4149 (1997).
[12] J.F. Lawler, R. Schad, S. Jordan, and H. van Kempen, J. Magn. Magn. Mater. **165**, 224 (1997).
[13] J.C. Slonczewski, Phys. Rev. Lett. **67**, 3172 (1991).
[14] S. Demokritov, E. Tsymbal, P. Grünberg, W. Zinn, and I.K. Schuller, Phys. Rev. B **49**, 720 (1994).
[15] J.C. Slonczewski, J. Magn. Magn. Mater. **150**, 13 (1995).
[16] D.E. Bürgler, C.M. Schmidt, J.A. Wolf, T.M. Schaub, and H.-J. Güntherodt, Surf. Sci. **366**, 295 (1996).
[17] D.E. Bürgler, P. Hermann, S. Corbel, C.M. Schmidt, D.M. Schaller, P. Sautet, A. Baratoff, and H.-J. Güntherodt, Phys. Rev. B **57**, 10 035 (1998).
[18] A. Davies, J.A. Stroscio, D.T. Pierce, and R.J. Celotta, Phys. Rev. Lett. **76**, 4175 (1996).
[19] D. Venus and B. Heinrich, Phys. Rev. B **53**, R1733 (1996).
[20] J.A. Stroscio, D.T. Pierce, and R.A. Dragoset, Phys. Rev. Lett. **70**, 3615 (1993).
[21] M. Rührig, R. Schäfer, A. Hubert, R. Mosler, J.A. Wolf, S. Demokritov, and P. Grünberg, Phys. Status Solidi A **125**, 635 (1991).
[22] R. Schäfer, J. Magn. Magn. Mater. **148**, 226 (1995).
[23] G. Ehrlich and F.G. Hudda, J. Chem. Phys. **44**, 1039 (1966).
[24] R.L. Schwoebel and E.J. Shipsey, J. Appl. Phys. **37**, 3682 (1966).
[25] J.A. Stroscio and D.T. Pierce, Phys. Rev. B **49**, 8522 (1994).
[26] J.G. Amar and F. Family, Phys. Rev. B **52**, 13 801 (1995).
[27] C. M. Schmidt, Ph.D. thesis, University of Basel, 1998.
[28] A. Schreyer, J.F. Anker, Th. Zeidler, H. Zabel, C.F. Majkrzak, M. Schäfer, and P. Grünberg, Europhys. Lett. **32**, 595 (1995).
[29] A. Schreyer, J.F. Ankner, Th. Zeidler, H. Zabel, M. Schäfer, J.A. Wolf, P. Grünberg, and C.F. Majkrzak, Phys. Rev. B **52**, 16 066 (1995).

[30] J.A. Stroscio, D.T. Pierce, J. Unguris, and R.J. Celotta, J. Vac. Sci. Technol. B **12**, 1789 (1994).

[31] B. Heinrich, J.F. Cochran, D. Venus, K. Totland, D. Atlan, S. Govorkov, and K. Myrtle, J. Appl. Phys. **79**, 4518 (1996).

[32] Note that the STM images $z_{Fe}(x,y)$ and $z_{Cr}(x',y')$ are taken at different spots of the sample surface. However in the case of uncorrelated roughness it is legitimate to subtract *any* STM detail image of the bottom Fe surface from *any* detail image of the Cr surface to get a *statistical* representation of the Cr thickness fluctuations. Therefore, we may set $x'=x$ and $y'=y$.

[33] J.C. Slonczewski, B. Patek, and B.E. Argyle, IEEE Trans. Magn. **24**, 2045 (1988).

[34] M. Rührig and A. Hubert, J. Magn. Magn. Mater. **121**, 330 (1993).

[35] M. Labrune and J. Miltat, IEEE Trans. Magn. **29**, 2569 (1993).

[36] R. Ribas and B. Dieny, Phys. Lett. A **167**, 103 (1992).

[37] H. Zabel, A. Schreyer, P. Boedecker, and P. Sonntag, in *Dynamical Properties of Unconventional Magnetic Systems*, Vol. 349 of NATO Advanced Study Institute, Series E: Applied Sciences (Kluwer, Dordrecht, 1998), p. 239.

[38] P. Bruno and C. Chappert, Phys. Rev. B **46**, 261 (1992).

[39] D.G. Laurent, J. Callaway, J.L. Fry, and N.E. Brener, Phys. Rev. B **23**, 4977 (1981).

[40] Y. Wang, P.M. Levy, and J.L. Fry, Phys. Rev. Lett. **65**, 2732 (1990).